Research article

Simone Zanotto*, Giacomo Mazzamuto, Francesco Riboli, Giorgio Biasiol, Giuseppe C. La Rocca, Alessandro Tredicucci and Alessandro Pitanti

Photonic bands, superchirality, and inverse design of a chiral minimal metasurface

https://doi.org/10.1515/nanoph-2019-0321
Received August 21, 2019; revised September 29, 2019; accepted September 29, 2019

Abstract: Photonic band structures are a typical fingerprint of periodic optical structures, and are usually observed in spectroscopic quantities such as transmission, reflection, and absorption. Here we show that the chiro-optical response of a metasurface constituted by a lattice of non-centrosymmetric, L-shaped holes in a dielectric slab shows a band structure, where intrinsic and extrinsic chirality effects are clearly recognized and connected to localized and delocalized resonances. Superchiral near-fields can be excited in correspondence to these resonances, and anomalous behaviors as a function of the incidence polarization occur. Moreover, we have introduced a singular value decomposition (SVD) approach to show that the above mentioned effects are connected to specific fingerprints of the SVD spectra. Finally, by means of an inverse design technique we have demonstrated that the metasurface based on an L-shaped hole array is a minimal one. Indeed, its unit cell geometry depends on the smallest number of parameters needed to implement arbitrary transmission matrices compliant with the general symmetries for 2d-chiral structures. These observations enable more powerful wave operations in a lossless photonic environment.

Keywords: metasurface; polarization; chirality; inverse design.

***Corresponding author: Simone Zanotto,** Istituto Nanoscienze – CNR and Laboratorio NEST, Scuola Normale Superiore, Piazza San Silvestro 12, 56127 Pisa, Italy, e-mail: simone.zanotto@nano.cnr.it. https://orcid.org/0000-0001-7180-3335
Giacomo Mazzamuto and Francesco Riboli: European Laboratory for Non Linear Spectroscopy, via N. Carrara 1, Sesto Fiorentino, Firenze 50019, Italy; and CNR-INO Sesto Fiorentino, via Nello Carrara 1, Firenze 50019, Italy
Giorgio Biasiol: Istituto Officina dei Materiali CNR, Laboratorio TASC, Basovizza (TS), Italy
Giuseppe C. La Rocca: Scuola Normale Superiore and CNISM, Piazza dei Cavalieri 7, 56126 Pisa, Italy
Alessandro Tredicucci: Istituto Nanoscienze – CNR and Laboratorio NEST, Scuola Normale Superiore, Piazza San Silvestro 12, 56127 Pisa, Italy; and Dipartimento di Fisica "E. Fermi", Università di Pisa, Largo Pontecorvo 3, 56127 Pisa, Italy
Alessandro Pitanti: Istituto Nanoscienze – CNR and Laboratorio NEST, Scuola Normale Superiore, Piazza San Silvestro 12, 56127 Pisa, Italy

1 Introduction

Electromagnetic fields which carry chirality – in their simplest form, left- and right-circularly polarized plane waves – deserve huge interest as they interact with matter chirality, enabling for instance to discriminate enantiomers in chemistry, which are ultimately connected with key features of living organisms. Indeed, many biomolecules have a specific handedness (*homochirality*), and it is not yet clear why nature has decided to go in that precise direction [1]. From a more application-oriented point of view, the pharmaceutical industry constantly seeks for effective methods to discriminate stereoisomers, an application where chiral light-matter interaction could prove useful.

To date, the most common technique to prepare and analyze chiral light is to employ birefringent plates and linear polarizers that convert light to and from linear polarization, as the technology of direct sources and detectors of chiral light is still in its infancy [2–5]. Last advances in nanotechnology are however revolutionizing chiral optical devices [6–17]. Far- and near-field chiral electromagnetic responses have been indeed observed in a variety of artificially structured systems, where the shape of the machined elements must have a three-dimensional character if geometric and electromagnetic chirality has to be attained in its most rigorous form, because

of the requirement of the absence of any mirror symmetry plane [18–21]. Several proposed structures hence rely on volumetric fabrication techniques, which however suffer from either scarce throughput or limited flexibility. Thus, less demanding fabrication technologies – i.e. planar technologies – may also be employed, as witnessed by some reports [22–24]. For instance, a dielectric film with a non-centrosymmetric partially etched planar pattern was proposed as a simple gateway towards strong chiro-optical phenomena [25]. Indeed, there is a wide interest in developing subwavelength-patterned high-index dielectrics, both for applications and for fundamental research: from one side, they enable the synthesis of flat lenses, polarimeters, spectrometers, nonlinear components and computer-generated holograms [26–33]; from another side, they exhibit a variety of intriguing phenomena such as Fano lineshapes, perfect forward scattering, geometric phase effects, and bound states in the continuum resonances [34–40].

Most of these effects arise from complex electromagnetic behaviors whose essence can be grasped understanding the interplay between localized and delocalized resonances. In other words, these systems often rely on the co-presence, and on the competition, between guided wave phenomena and antenna-like responses, as highlighted by the prototypical transition between the guided mode filter regime, the photonic crystal regime, and the independent-particle Mie-scattering regime [41]. In this work we have reported on the observation of photonic bands in a chiral metasurface, highlighting that the chiral response shows fingerprints of both guided wave and locally resonant phenomena. The object under investigation is the simplest conceivable 2d-chiral dielectric metasurface: a slab perforated with L-shaped holes [42]. In general, a 2d-chiral object is defined as follows: given the family Π of planes perpendicular to a given plane π_z (the subscript z refers to the fact that π_z is usually chosen to be a constant-z plane), an object is 2d-chiral if it cannot be superimposed with itself after a mirror reflection for any plane belonging to Π. A 2d-chiral object is also 3d-chiral if it cannot be superimposed with itself after a mirror reflection for any plane parallel to π_z. An object that is 2d-chiral but not 3d-chiral has a mirror symmetry plane of the type π_z. 2d-chiral objects may have vanishing or finite thickness along z. Our metasurface has a finite thickness; this property allows it to implement interesting chiral electromagnetic features such as chiro-optical far-field response at normal incidence [19]. To our knowledge, our work is the first report of a 2d-chiral, 3d-achiral, dielectric metasurface; moreover, it is the first report of angularly-resolved spectroscopy of 2d-chiral, 3d-achiral metasurfaces. The metasurface under analysis also exhibits superchiral near-fields with incident unpolarized light. The response at normal incidence will be analyzed by means of a singular-value decomposition approach that reveals the operational capabilities of any 2d-chiral photonic device. In addition, we have shown that the extremely simple L-shaped structure is also a *minimal* one: by tuning a small number of geometrical parameters, it is possible to access a very wide set of the transmission matrices characteristic of a general 2d-chiral metasurface. In this sense, we approached the solution of the inverse design problem of 2d-chiral metasurfaces [43].

2 Chiral response at normal incidence

The metasurface under investigation is illustrated in Figure 1A. It consists of a 220 nm thick gallium arsenide membrane, patterned with L-shaped holes arranged over a square lattice. The geometric parameters of the holes are reported in Figure 1B, superimposed to the scanning electron microscope (SEM) image of a fabricated sample. While in forthcoming analysis the parameters a, $f_1 \ldots f_4$ are allowed to vary, the first part of the article deals with a specific choice of parameters, which correspond indeed to the SEM image. In detail, we have $a = 1134$ nm, $f_1 = 0.76$, $f_2 = 0.58$, $f_3 = f_4 = 0.327$. The sample fabrication process, whose details are reported in the Supplementary Materials, allows to obtain a frame-supported membrane, freely accessible from both sides to perform optical measurements with a moderately focused (≈50 μm spot) near-infrared (1–2 μm wavelength) beam. The beam originates from a supercontinuum source, filtered by means of an acousto-optic tunable filter yielding a spectral bandwidth of ≈2 nm. The system is controlled through an automated software developed in C++. The polarization state is prepared with a Glan-Taylor polarizer followed by a $\lambda/4$ superachromatic waveplate; no polarization analysis was performed on the beam transmitted after the sample. The sample was mounted on a rotating support that enables to measure the angularly-resolved transmittance, as illustrated in Figure 1A. A first set of measurements has been collected at normal incidence ($\alpha = 0$). The experimental data are reported in Figure 1C, and are compared with the outcome of a numeric model (rigorous coupled wave analysis, RCWA

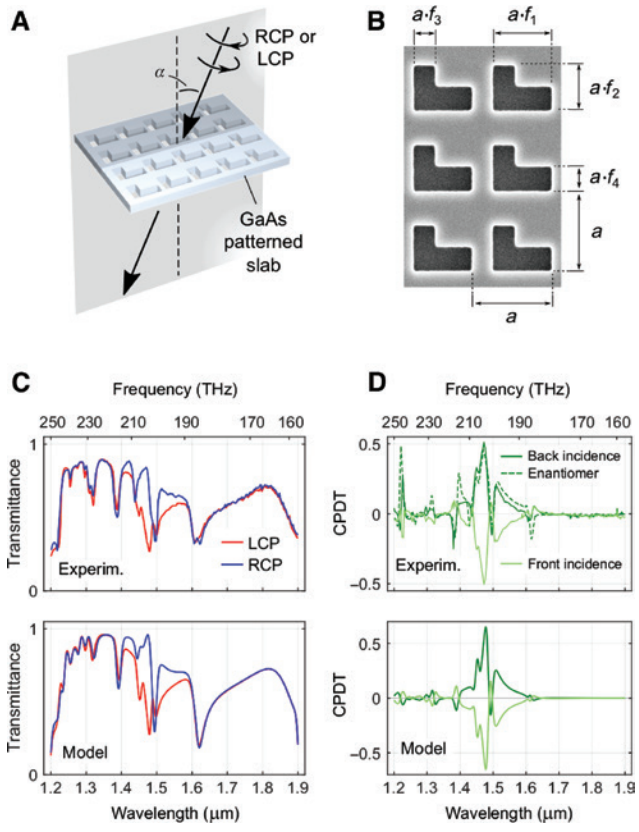

Figure 1: (A) Schematic representation of the metasurface and the optical measurement. RCP and LCP indicates right- and left-circularly polarized light, respectively. (B) Scanning electron micrograph of the metasurface with its geometrical parameters. (C) Polarization-resolved transmittance spectra, both from the experiment and the numerical modeling. (D) Circular polarization differential transmittance CPDT (i.e. difference between LCP and RCP transmittances) measured on the metasurface represented in (B) from both front and back side, and from the front side of a metasurface having the enantiomeric pattern (see text for details).
Data in panels (C) and (D) are obtained at $\alpha = 0$.

– see the Supplementary Materials for details). The spectra consist of a series of quite narrow dips, some of them having different shapes and depths depending on the polarization state of the incident light. From the transmittances for left (right) circularly polarized light, respectively $\mathcal{T}_L$ ($\mathcal{T}_R$), the circular polarization differential transmittance can be defined as CPDT $= \mathcal{T}_L - \mathcal{T}_R$: this quantity is plotted in Figure 1D. Here, the traces labeled *front incidence* and *back incidence* have been collected from the same sample, but illuminated from either the top surface or the bottom surface. The trace *enantiomer* derives instead from a second sample, which differs from the first one solely for the L-shaped hole sense of chirality at fabrication stage: the second sample, when observed from the front side, is described by the same parameters of the first sample exception made for the exchange $f_1 \leftrightarrow f_2$. A good matching between the CPDT spectrum of the enantiomer with that of the original sample's back side, as well as the fact that the front and back side CPDT are opposite to each other, indicates that the objects under investigation are almost perfectly 2-d chiral. Indeed, while in principle a through-hole perforated homogeneous membrane has a mirror plane parallel to its surface, fabrication imperfections may have lead the actual sample to deviate from this ideal characteristic. The data indicate instead that the two samples are essentially the same object, from both geometric and electromagnetic points of view.

The data reported so far indicate that a 2d-chiral metasurface with a very simple design exhibits strong circular polarization differential transmittance in a narrow band close to the optical telecommunication window. It should be emphasized that the observed CPDT is not accompanied by absorption; rather, it originates from a redistribution of the incident energy among the transmitted and reflected beams (no diffraction is present, thanks

to the subwavelength dimensions of the pattern). In this sense, the presented object is rather a beam splitter sensitive to the circular polarization, and the observed CPDT is inherently different from the absorption circular dichroism (or circular diattenuation, CD), properly occurring, for instance, in isotropic solutions of chiral molecules. However, from an observer point of view who can only access the transmitted beam, CPDT is indistinguishable from CD. Hence, our metasurface can be employed to mimick the CD of target objects, such as naturally occurring molecules.

3 Chiral response at oblique incidence and band structure

In the transmission spectra reported in Figure 1, a rich structure can be noticed, whose physical origin deserves attention *per se* and in view of applications. In order to get further insight into the nature of the resonances leading to CPDT peaks, a powerful method is to measure the metasurface transmittance at different angles of incidence (i.e. for different orientations of the incident wavevector). Angularly-resolved measurements have been recently employed to reveal special features of polarization phenomena like magneto-optic effects in quasi-ordered structures [44] and asymmetric transmission in low-symmetry plasmonic hole arrays [45]. With angularly-resolved measurements, one may distinguish between dispersive and non-dispersive resonances, which originate from different physical phenomena: guided mode resonances and antenna-like resonances, respectively. In Figure 2A and B, we have reported the CPDT mapped in the frequency-wavevector space for our metasurface. Here, the in-plane wavevector is the projection of the incident light wavevector on the metasurface plane. In the experiment only positive angles have been studied, while the model data are available for both positive and negative angles. The good matching between experimental and model data allows to acquire confidence in the model as a whole, which shows interesting features. First, strongly dispersive bands, with positive and negative slope, suggest that the metasurface optical response has important contributions from guided mode resonances (also known as quasi-guided modes); this picture is supported by an empty-lattice band-folding model illustrated in the Supplementary Material. These

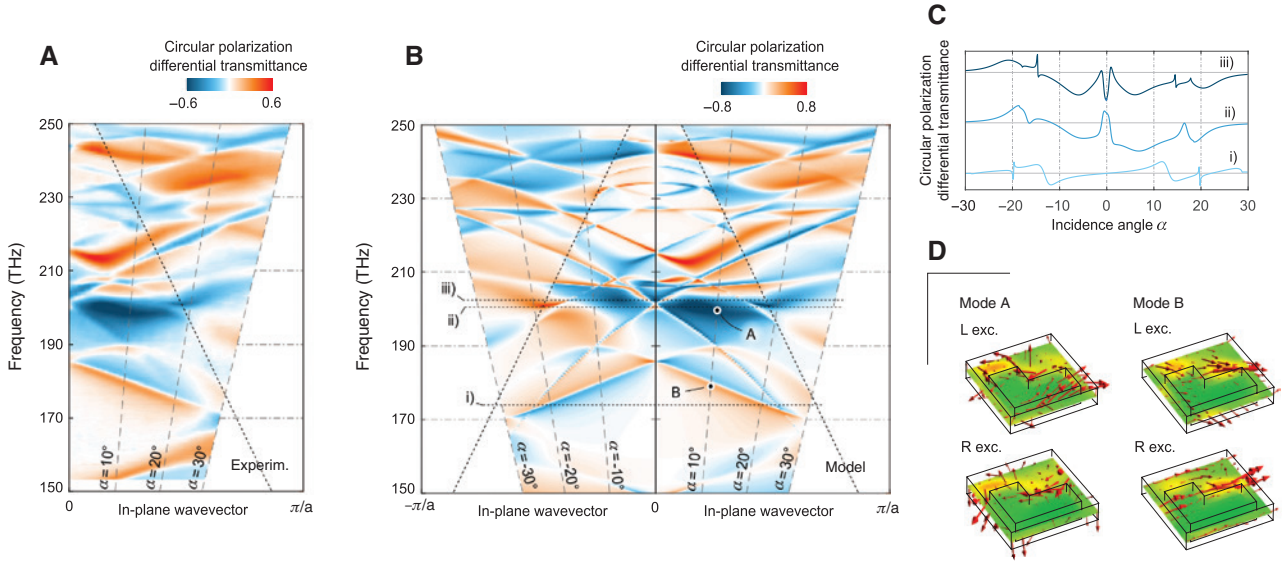

Figure 2: The CPDT mapped in the frequency-wavevector space for our metasurface.
Measured (A) and modeled (B) circular polarization differential transmittance (CPDT) band structure of the metasurface. A rich pattern originating from the interplay between guided mode resonances and antenna-like resonances is observed. The diagonal short-dash lines represent the diffraction threshold: below those lines the sample operates in the proper metasurface regime. By tuning the incidence angle α the first Brillouin zone is probed along a high-symmetry direction (see also Figure 1A). Notice that the CPDT does not fulfil the relation CPDT(α) = −CPDT(−α). Panel (C) highlights this behavior, for three optical frequencies identified in panel (B). Panel (D) illustrates the electromagnetic energy density (color map: green = low, orange = high) and the Poynting vector (red arrows) inside the metasurface unit cell for modes A and B (see panel (B) for their definition) and for both circular polarization states of the illuminating beam. Notice that in mode B the Poynting vector follows a well-defined direction, witnessing the presence of a traveling wave, while in mode A it "winds up" around the L-shaped inclusion, indicating a localized resonance.

resonances are responsible for the narrow dips observed in the transmission spectra and for the sharp oscillations in the CPDT spectra.

Second, by comparing the CPDT observed at opposite angles, it can be noticed that in the region at the center of the map ($-20° < \alpha < 20°$, 190 THz $< \nu <$ 210 THz) the CPDT is not symmetric with respect to the exchange $\alpha \leftrightarrow -\alpha$. The effect can be better noticed looking at the curves in Figure 2C, where the CPDT as a function of the incidence angle has been reported for three fixed values of light frequency (labels i–iii in the figure). We attribute this effect to the presence of a spectrally and angularly broad chiral resonance, which we referred to as L-hole resonance. This resonance has a behavior that contrasts in two ways that of the guided mode resonances: first, the broad angular response of the L-hole resonance suggests that it has a spatially localized nature, as opposed to the delocalized, traveling-wave nature of the guided mode resonances (which instead follow a dispersive energy-wavevector curve). Second, the L-hole resonance induces the property $\mathrm{CPDT}(\alpha) \neq -\mathrm{CPDT}(-\alpha)$ (observed in the central region of the map, around point A in Figure 2B), while the guided-mode resonances display $\mathrm{CPDT}(\alpha) = -\mathrm{CPDT}(-\alpha)$ (dispersive bands, point B).

Seeking for further confirmation of this view, we have calculated (see the Supplementary Materials for details) the optical near fields of the metasurface unit cell, upon the illumination conditions that excite the two types of resonances. The data are plotted in Figure 2D, where both the energy density (color map) and the Poynting vector (arrows) are reported. While the energy density distributions do not show remarkable behaviors, the Poynting vector field shows interesting properties that are consistent with the picture sketched above. When the metasurface is illuminated with the energy-wavevector pair labeled as "A" in Figure 2B, the Poynting vector in the unit cell has a strongly inhomogeneous distribution: for left polarized excitation, it even "winds up" around the L-shaped hole. For right-polarized excitation the Poynting vector has a different, yet irregular, distribution. We have interpreted these irregular distributions as arising from the L-hole resonance: a localized resonance dominated by multipoles, similar to the reports of [25]. On the contrary, when the metasurface is illuminated with the energy-wavevector pair labeled "B", the Poynting vector shows much more regular distributions, typical of a guided mode that propagates parallel to the slab. Noticeably, the direction of the Poynting vector is opposite with respect to that of the in-plane wavevector, consistently with the negative dispersion of the photonic band where point B lies on.

4 Superchiral near-fields

Besides far-field angularly-dispersive chiro-optic response, which is of interest – for instance – for filters, holograms, and multiplexers, near-field optical chirality plays a fundamental role in the interaction with chiral matter. First relegated to the role of pure mathematical curiosity, electromagnetic (e.m.) chirality is now regarded as a crucial quantity to be taken care of when the optical detection of chiral molecules is under investigation [46–50]. The ability of a photonic structure to enhance the e.m. chirality is quantified by the *normalized e.m. chirality*, defined as $\hat{C} = -c\ \mathrm{Im}(\mathbf{E}^* \cdot \mathbf{B})/|\mathbf{E}_{\mathrm{inc}}|^2$, where c is the speed of light, $\mathbf{E}$ and $\mathbf{B}$ are the fields at the point of interest, and $\mathbf{E}_{\mathrm{inc}}$ is the electric field vector of the incident plane wave. In the absence of any photonic structure, the plane wave would freely propagate and one would have $\hat{C} = 0$ for linear polarization and $\hat{C} = \pm 1$ for right (left) circular polarization. When the incident wave impinges instead on a photonic structure, the near-fields excited in its vicinity may display a significantly different value of $\hat{C}$: for instance, one may have $\hat{C} \neq 0$ also if the incident light is linearly polarized, or it is possible that $|\hat{C}| \gg 1$ (*superchiral field*). Figure 3 shows that the 2d-chiral L-shape patterned membrane has a strong near-field e.m. chirality, also at normal incidence, and also when considering the spatial average of $\hat{C}$ over a plane placed in closed proximity of the metasurface

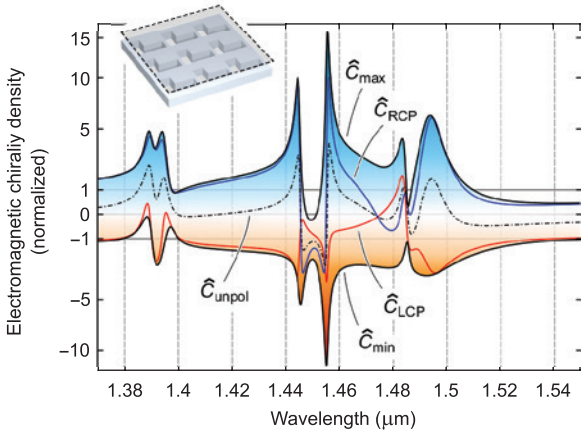

Figure 3: Simulated electromagnetic chirality density $\hat{C}$ calculated by averaging the local chirality density on a plane above the metasurface (see the figure inset and the main text for details). The different traces report the values of $\hat{C}$ that can be attained upon different incident polarization conditions: left- and right-circular (LCP and RCP) and unpolarized (*unpol*). $\hat{C}_{\mathrm{max}}$ and $\hat{C}_{\mathrm{min}}$ are the absolute maximum and minimum attainable values of $\hat{C}$; they correspond, in general, to an elliptical polarization state of the incident light. Normal incidence is assumed. Free-space propagating RCP and LCP have $\hat{C} = \pm 1$, respectively.

(figure inset). In the graph, the colored area indicates the accessible values of $\hat{C}$ for the present structure. Superchiral behavior occurs at wavelengths corresponding to the spectral features observed in the far-field transmission (see Figure 1C). Noticeably, maximum (minimum) values of $\hat{C}$ are not always achieved upon right (left) circularly polarized illumination, as it can be observed from the corresponding traces (blue and red curves, respectively). Even more curiously, at the wavelength of 1.48 μm a reversal occurs ($\hat{C}_{\mathrm{RCP}} < \hat{C}_{\mathrm{LCP}}$). Furthermore, a strongly anomalous value $\hat{C}_{\max} < 0$ is observed at $\lambda = 1.45\,\mu\mathrm{m}$. We have attributed these anomalies to the influence of the chiral localized resonance, "mode A", discussed above, whose interplay with the narrower guided mode resonances leads to such features. In the considered spectral region other interesting phenomena take place. First, the metasurface displays $\hat{C} \neq 0$ also when it is illuminated with unpolarized light, as illustrated by the trace $\hat{C}_{\mathrm{unpol}}$. Second, the definite chirality of the metasurface enables an asymmetry between the extreme values of $\hat{C}$, which do not fulfil the equality $\hat{C}_{\max} = -\hat{C}_{\min}$. In essence, an appropriate choice of the wavelength allows to engineer the near-field chiral response to a large extent, as the device response breaks certain conventional rules concerning e.m. chirality.

5 Singular value decomposition analysis of the metasurface operation

We will now focus back to the far-field metasurface response, in the attempt to understand in a comprehensive way its amplitude, phase, and polarization response. This analysis relies on the properties of the *T*-matrix (transmission matrix, or Jones matrix), where the device response concerning light transmission is completely encoded.[1] The *T*-matrix can be written over different bases; the most common choices being that of linearly or circularly polarized waves. The following Section identifies the *T*-matrix written in these bases as T_{L} and T_{C}, respectively. For instance, T_{C} operates over Jones vectors whose elements are the right- and left-handed circularly polarized components of incident/transmitted light: $\mathbf{t} = T_{\mathrm{C}}\mathbf{i}$, with $(\mathbf{t} = t_R, t_L)$ and $\mathbf{i} = (i_R, i_L)$.

The form of *T*, and hence the possible operations that a metasurface can implement, are dictated by geometrical symmetry properties of the pattern lattice and unit cell. For instance, the L-shaped hole structure belongs to the more general category of objects that have a single mirror symmetry plane π_z (see Section 1); these objects are usually said to belong to the $M_{x,y}$ symmetry class. Under normal incidence, the T_{L} matrix of such metasurface is symmetric: $T_{\mathrm{L}} = T_{\mathrm{L}}^{t}$ [42]. However, to get a more insightful vision into the metasurface operation we found it useful to focus on the properties of T_{C}, in particular to its singular value decomposition (SVD). The SVD is an algebraic operation that reveals the structure of non-unitary linear operators, similarly to what eigenvalue decomposition (ED) does about unitary operators; a short recall of the properties of the SVD are given in the Supplementary Material. In the case under analysis we believe that the SVD is better suited with respect to ED, since the *T*-matrix is in general non-unitary. Indeed, a dielectric metasurface is lossless in its full response (reflection plus transmission), but it appears lossy as the sole transmission is considered. The SVD of *T* naturally describes the energy-handling behavior of the metasurface, since the square of its two singular values are the maximum and minimum wave intensity that can be transmitted by the metasurface (assuming unit intensity incident beam) [51]. Thus, our approach goes beyond what was reported in past studies on planar chiral metamaterials which did not rely on the SVD [52, 53], although an application of SVD to Müller-Jones calculus, not specific for chiral materials, is reported in [54]. We thus believe that SVD of chiral metasurfaces may provide a complementary viewpoint with respect to other decomposition methods (pseudopolar and integral decomposition [55, 56]) employed in polarization optics.

Algebraic manipulations (see the Supplementary Material) leveraging on the symmetry of T_{L} imply that the unitary matrices *V* and *W* appearing in the SVD of T_{C}, i.e. $T_{\mathrm{C}} = \mathrm{V}\Sigma\mathrm{W}^{\dagger}$, must fulfil $\bar{V}W = \begin{pmatrix} 0 & 1 \\ 1 & 0 \end{pmatrix}$. We recall that Σ is a diagonal matrix containing the singular values $\sigma_{1,2}$, and that the notation $\bar{V}$ indicates the element-wise matrix complex conjugate. The constraint on *V* and *W* implies that these matrices can be parametrized in the following insightful form:

$$V = -ie^{i\tilde{\varphi}/2} D_1 O D_2, \qquad W = e^{-i\tilde{\varphi}/2} D_1' O' D_2'$$

where

$$D_1 = D_1' = \begin{pmatrix} e^{i\psi} & 0 \\ 0 & e^{-i\psi} \end{pmatrix}, \qquad O = \begin{pmatrix} \sin\theta & \cos\theta \\ -\cos\theta & \sin\theta \end{pmatrix},$$

$$O' = \begin{pmatrix} \cos\theta & \sin\theta \\ -\sin\theta & \cos\theta \end{pmatrix}, \quad D_2 = \begin{pmatrix} -ie^{-i\Delta} & 0 \\ 0 & ie^{i\Delta} \end{pmatrix}, \quad D_2' = \begin{pmatrix} e^{i\Delta} & 0 \\ 0 & e^{-i\Delta} \end{pmatrix}.$$

With this notation one has $T_{\mathrm{C}} = D_1 F D_1^{\dagger}$, which means that the metasurface performs a "core" operation, described

1 We recall that we are limiting ourselves to the regime where the wavelength is larger than the pattern periodicity, i.e. to the *metasurface regime*, where no diffraction takes place.

by F, transformed by the basis change identified by the unitary matrix D_1. Noticeably, D_1 is the matrix that describes, in the circular polarization basis, a rotation of the reference system about the axis perpendicular to the metasurface plane. In other words, the operation of an $M_{x,y}$-symmetric metasurface can be summarized in the operation encoded by the operator $F = -ie^{i\tilde{\phi}} O D_2 \Sigma D_2'^{\dagger} O'^{t}$, that however acts in a rotated coordinate system. From this fact it follows that, in order to specify the operation of a $M_{x,y}$-symmetric metasurface, it is sufficient in essence to specify its F: after that, the full space of transmission matrices can be saturated by simply rotating the metasurface about the axis perpendicular to the metasurface plane. It should be noticed that the above parametrization involves six real parameters, consistently with the fact that we are describing the symmetric Jones matrix T_L.

We now pay attention to understand the meaning of the parameters entering the matrices introduced above. To this end one should explicitly describe the operation of T_C over a generic incident field vector $\mathbf{i}$. By decomposing it over the basis defined by the columns $\mathbf{w}^{(1,2)}$ of the unitary matrix W, one has $T_C\mathbf{i} = T_C(i_1\mathbf{w}^{(1)} + i_2\mathbf{w}^{(2)}) = \sigma_1 i_1 \mathbf{v}^{(1)} + \sigma_2 i_2 \mathbf{v}^{(2)}$. With these expressions the metasurface operation can be directly visualized on the Poincaré sphere, as illustrated in Figure 4. In essence, the metasurface decomposes the incident polarization state over the polarization states identified by $\mathbf{w}^{(1,2)}$, reverses the handedness of these states (by converting $\mathbf{w}^{(1,2)} \to \mathbf{v}^{(1,2)}$), and scales the energy content of each polarization state, according to the singular values $\sigma_{1,2}$. The location of the polarization states is connected with the parameters ψ and θ that appear in the matrix decomposition reported above (Figure 4). As expected, ψ is connected to a physical rotation (a rotation in the plane of the coordinate axes identifying the x- and y-related Stokes parameters $S_{1,2}$). Instead, θ is directly connected with the "chiral" Stokes parameter S_3. In the following, we mostly dropped the use of θ and rather defined the metasurface functionality referring to the S_3 values of $\mathbf{w}^{(1,2)}: S_3^{(1,2)} = \pm\cos 2\theta$.

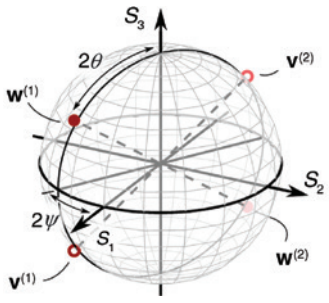

Figure 4: Illustration of the action of a 2d-chiral metasurface on the Poincaré sphere. $\mathbf{w}^{(1,2)}$ and $\mathbf{v}^{(1,2)}$ identify the polarization states of, respectively, right and left singular vectors of the transmission (Jones) matrix.
The metasurface operation is to map the **w**'s into the **v**'s, plus a rescaling described by the singular values (see text for details).

To complete the picture one should also consider the phase response of the metasurface, which is described by the parameters $\tilde{\phi}$ and Δ that appear in the decomposition. These parameters are connected to a relative and a global phase, in the following sense: Δ identifies the phase difference between the R components of $\mathbf{w}^{(1,2)}$, since $2\Delta = \arg(w_R^{(1)}) - \arg(w_R^{(2)})$. Instead, the phase difference between incident and transmitted field, $\phi = \arg(v_R^{(1)}) - \arg(w_R^{(1)})$ is given by $\phi = \tilde{\phi} - 2\Delta + \pi$. Both the relative and global phases are of practical interest, as they allow independent control over the phase profile of both polarizations in polarization-dependent metasurface holograms.

The algebraic and parametric analysis performed so far is valid at each individual wavelength. More information can however be obtained by studying the spectral dispersion of the SVD parameters, whose frequency-dependent response can be eventually correlated with quantities of more direct experimental access. In Figure 5A we have plotted the calculated spectral dispersion of the singular values for the L-shaped hole array described in the previous sections. The data follow from numerical SVD of the Jones matrix calculated from RCWA (see Supplementary Material); an experimental measurement of the SVD parameters is possible, in principle, relying on Müller-Jones polarimetry (exception made for the determination of ϕ that would require interferometry). In the analysis of Figure 5A singular values are not sorted in decreasing order, rather, they are sorted such as their trend with respect to the wavelength is smooth. The spectrum reveals a structure with narrow dips, mostly occurring in pairs, which stand out of a background where both σ's are close to 1 (for $\lambda < 1.45$ μm) or where one σ is close to 1 and the other is close to 0.5 ($\lambda > 1.45$ μm). Noticeably, these dips occur at the same wavelengths where the spectra of transmission, circular polarization differential transmittance, and near-field chirality also show peaks or dips. It is also interesting to notice that the dips reach zero at those wavelengths, the metasurface does not transmit the radiation which is incident with the polarization dictated by the corresponding right singular vector. Figure 5B reports the spectral dependence of the third Stokes parameter of the right singular vectors. Here it can be noticed that the $S_3^{(1,2)}$ spectra show a large peak centered around 1.47 μm: this feature clearly recalls the localized, broadband resonance discussed in Section 3. On top of that, narrow features, of widths comparable to those observed in $\sigma_{1,2}$, are present.

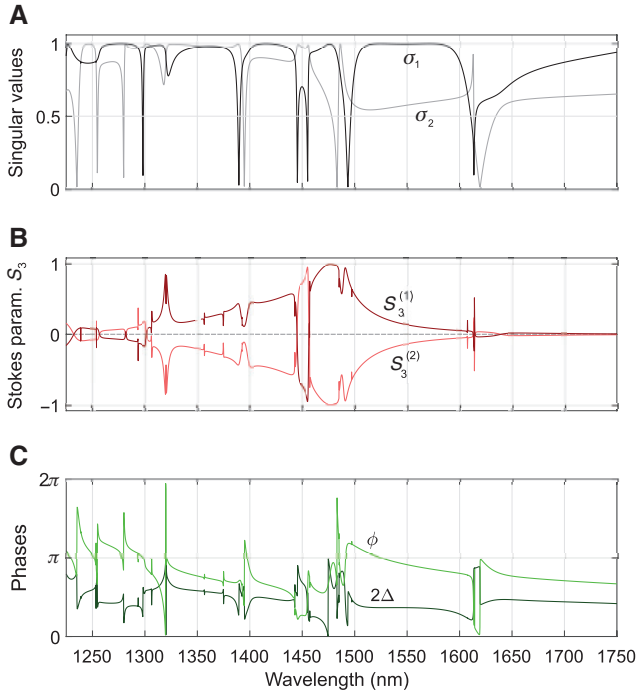

Figure 5: Main quantities arising from the singular value decomposition (SVD) of the metasurface transmission matrix at normal incidence.
Panel (A), singular value spectra. Note that the singular values structures recall the features observed in the transmittance, circular polarization differential transmittance and electromagnetic chirality spectra (Figures 1 and 3). Panel (B), third component of the Stokes parameter of the right singular vector. $S_3^{(1,2)}$ correspond, respectively, to singular values $\sigma_{1,2}$. Panel (C), relative phase 2Δ (i.e. phase between right singular vectors) and absolute transmission phase ϕ.

Finer features, often occurring close to the points where $\sigma_1 = \sigma_2$, have an unclear interpretation and may be connected to singular value degeneracy. In the wavelength region around 1.45 μm a reversal of the signs of $S_3^{(1,2)}$ was also observed. The spectral features present on $\sigma_{1,2}$ and on $S_3^{(1,2)}$ clearly recall what noticed on the observables that have been studied in the previous sections (transmission, circular polarization differential transmittance, and near-field chirality): we have attributed this fact to the presence of a common ground – i.e. metasurface resonances – standing behind all these phenomena. We have finally reported in Figure 5C the spectra of the phases ϕ and 2Δ, which also show a rich behavior, with rapid changes occurring close to the zeros of the singular values. In general, the spectral behavior of the SVD parameter is rather complex. While this fact, from one side, opens further challenges in view of a comprehensive interpretation, it also holds promises in view of metasurface engineering: in essence, there is a wide space where the metasurface functionality can be chosen and designed.

6 Inverse problem and metasurface minimality

Provided with the SVD formalism, and motivated by the conclusions of the previous Section, an intriguing question is whether it is possible to solve the inverse problem: given a target metasurface function (i.e. a target T matrix, or better a set of target parameters $\sigma_{1,2}$, $S_3^{(1)}$, Δ, ϕ, and ψ), does it exist a metasurface unit cell shape that induces it? We have determined that appropriately shaped L-holes in a 220 nm thick dielectric slab with a refractive index n = 3.38 (i.e. that of GaAs at 1.55 μm), are capable of implementing an arbitrary T matrix of the class pertinent to $M_{x,y}$ objects. In this analysis the technologically relevant case of normal incidence is assumed. We approached the inverse problem by choosing a large set (120 combinations) of target parameters; the complete list is reported in the Supplementary Material. By running an optimization algorithm we have been able to identify, for all the targets, a specific geometry of the L-shaped hole such that the calculated T matrix matches the target. It is interesting to notice that the L-shaped hole has 5 degrees of freedom (a, $f_1 \ldots f_4$), the same as the number of non-trivial degrees of freedom of the T matrix of $M_{x,y}$ objects: $\sigma_{1,2}$, $S_3^{(1)}$, Δ and ϕ. In this sense we have defined the metasurface as *minimal*. We recall that the parameter ψ is trivial in the sense defined in the previous Section, since it can be targeted by simply rotating the metasurface. While the complete solution dataset is available in the Supplementary Material, we have reported here four exemplary cases. Three of them are of immediate and intuitive interpretation; they are illustrated in Figure 6A–C. The target objects are polarizers, which are characterized by $\sigma_1 = 1$, $\sigma_2 = 0$. The first (A) is an ordinary circular polarizer, the second (B) is a circular polarizer that also imprints a phase delay, and the third (C) is an elliptical polarizer. More precisely, the objects under consideration are polarizers *and* handedness inverters: thanks to the special structure of the singular vectors, a $M_{x,y}$ object with $\sigma_1 = 1$ and $\sigma_2 = 0$ eliminates one of the polarization components of the incident field, and transmits the other with inverted handedness (see Figure 4 and the related discussion). The fourth example, Figure 6D, is an implementation of the most general type of T-matrices that can be targeted by means of $M_{x,y}$ objects. Here, all the target parameters ($\sigma_{1,2}$, $S_3^{(1)}$, Δ, ϕ) assume non-trivial values. The input and output singular states are elliptic polarization states, there is a phase difference between the input singular states, there is a phase difference between the output singular states, and the singular values are different from each other, and different

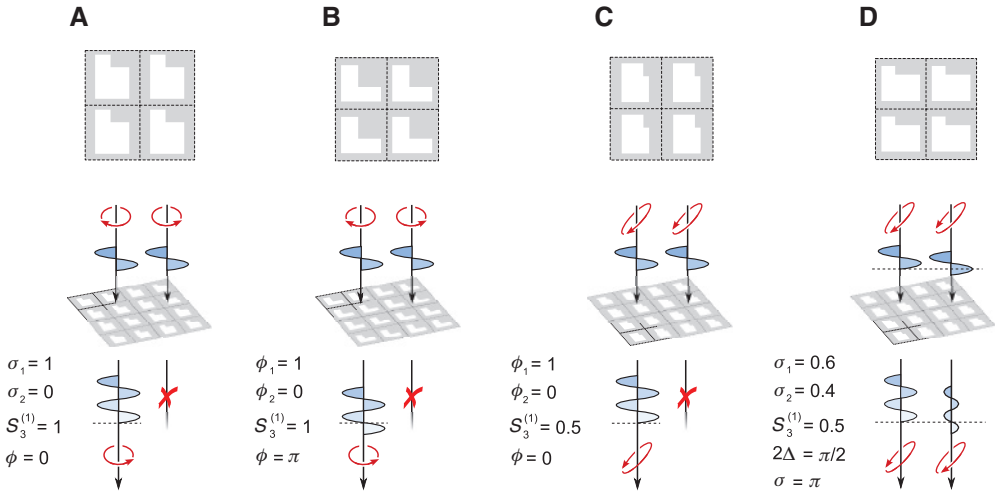

Figure 6: Example of wave operations achievable with the minimal metasurface: (A) circular polarizer, (B) circular polarizer plus phase delay, (C) elliptical polarizer, (D) elliptical diattenuator plus phase delay.
The L-shapes illustrated in the top of the figure depict the actual geometry required to implement the aforementioned operations. The exact values of the geometrical parameters (a, $f_1 \ldots f_4$) are given in the Supplementary Material. In correspondence to each case we have also reported the SVD parameters (see Section 5 for details). A much wider library of L-shapes that realize wave operation targets spanning the whole accessible transmission matrix space is reported in the Supplementary Material.

from 0 to 1. In other words the metasurface behaves as the combination of a diattenuator and a retarder acting over elliptical states. Implementing this operation by means of conventional optical elements would require a bulky stack of layers, which are here replaced by a simple, subwavelength film where the operation is fully encoded in the shape of the lithographically defined holes. Hence, one might envisage ultracompact and ultralight optical components acting over all the key parameters of light – amplitude, phase and polarization. What is more, the possibility to access the full T-matrix parameter space by means of a simple hole-shape tuning of a fixed-thickness membrane allows to implement space-variant metasurfaces capable of performing more advanced operations with respect to what is known to date [30] with possible applications to beam shaping, holography, and cryptography. As a final remark we have highlighted the targeting procedure, which was performed at a wavelength of 1.55 μm that is of direct interest to the telecommunication technology, is fully scalable, thanks to the scale invariance of Maxwell's equations.

7 Conclusions

In conclusion we have reported the observation of various chiro-optical phenomena occurring in a 2d-chiral patterned dielectric slab, i.e. in a patterned slab that exhibits a single mirror symmetry plane parallel to the slab itself. Circular polarization differential transmittance is arranged in dispersive bands, and shows the fingerprints of localized and delocalized photonic resonances. It is in particular the effect of a localized resonance that induces an intrinsic chiral response on the metasurface, with consequences on the near-field chirality that shows superchirality and other anomalous behaviors. Relying on the singular value analysis of the transmission matrix, we identified the key parameters describing in full the operation of a 2d-chiral slab. We also noticed connections between the singular value spectrum and the above cited phenomena. Finally, we showed that the L-shaped hole structure, i.e. the most intuitive 2d-chiral pattern, is also a minimal one, as it allows to implement arbitrary transmission matrices with a minimal number of parameters. This result about inverse design might open the way towards advanced space-variant metasurfaces that exploit in full explore the phase, amplitude, and polarization degrees of freedom of light.

Acknowledgements: We like to acknowledge Alberto Bordin, who participated in an early stage of the project, Stefano Luin (Scuola Normale Superiore, Pisa) for the support on data fitting, Francesca Bontempi (Scuola Superiore Sant'Anna, Pisa) for ellipsometric measurements of the dielectric thin film, Sara Nocentini and Lorenzo Pattelli (LENS, Firenze) for their useful discussions and precious support for the spectroscopic measurements. This work was in part supported by the European Commission through the project PHENOMEN (H2020-EU-713450).

Author contributions: S.Z. has conceived the research and performed the electromagnetic simulations and the SVD analysis. S.Z. has fabricated the metasurface, from a thin film grown epitaxially by G.B. The spectroscopic measurements have been performed by S.Z. with the support of G.M. and F.R. The data have been interpreted by all the authors. The manuscript has been written by S.Z., with comments by all the authors.

References

[1] Lough WJ, Wainer IW. Chirality in natural and applied sciences. Oxford, UK, Blackwell Science, 2002.
[2] Lobanov SV, Tikhodeev SG, Gippius NA, et al. Controlling circular polarization of light emitted by quantum dots using chiral photonic crystal slabs. Phys Rev B 2015;92:205309.
[3] Dyakov SA, Semenenko VA, Gippius NA, Tikhodeev SG. Magnetic field free circularly polarized thermal emission from a chiral metasurface. Phys Rev B 2018;98: 235416.
[4] Konishi K, Nomura M, Kumagai N, Iwamoto S, Arakawa Y, Kuwata-Gonokami M. Circularly polarized light emission from semiconductor planar chiral nanostructures. Phys Rev Lett 2011;106:057402.
[5] Söllner I, Mahmoodian S, Hansen SL, et al. Deterministic photon–emitter coupling in chiral photonic circuits. Nat Nanotechnol 2015;10:775–8.
[6] Pfeiffer C, Grbic A. Bianisotropic metasurfaces for optimal polarization control: analysis and synthesis. Phys Rev Appl 2014;2:044011.
[7] Zhao Y, Belkin M, Alù A. Twisted optical metamaterials for planarized ultrathin broadband circular polarizers. Nat Commun 2012;3:870.
[8] Zhao Y, Askarpour AN, Sun L, Shi J, Li X, Alù A. Chirality detection of enantiomers using twisted optical metamaterials. Nat Commun 2017;8:14180.
[9] Hentschel M, Schäferling M, Duan X, Giessen H, Liu N. Chiral plasmonics. Sci Adv 2017;3:e1602735.
[10] Kong X-T, Besteiro LV, Wang Z, Govorov AO. Plasmonic chirality and circular dichroism in bioassembled and nonbiological systems: theoretical background and recent progress. Adv Mat 2018;1:1801790.
[11] Asadchy VS, Díaz-Rubio A, Tretyakov SA. Bianisotropic metasurfaces: physics and applications. Nanophotonics 2018;7:1069.
[12] Tullius R, Karimullah AS, Rodier M, et al. "Superchiral" spectroscopy: detection of protein higher order hierarchical structure with chiral plasmonic nanostructures. J Amer Chem Soc 2015;137:8380–3.
[13] Schaeferling M, Engheta N, Giessen H, Weiss T. Reducing the complexity: enantioselective chiral near-fields by diagonal slit and mirror configuration. ACS Photonics 2016;3: 1076–84.
[14] Vázquez-Guardado A, Chanda D. Superchiral light generation on degenerate achiral surfaces. Phys Rev Lett 2018;120:137601.
[15] Shaltout A, Liu J, Kildishev A, Shalaev V. Photonic spin Hall effect in plasmon metasurfaces for on-chip chiroptical spectroscopy. Optica 2015;2:860–3.
[16] Liu L, Yang D, Wan W, Yang H, Gong Q, Li Y. Fast fabrication of silver helical metamaterial with single-exposure femtosecond laser photoreduction. Nanophotonics 2019;8:1087.
[17] Zhang R, Zhao Q, Wang X, Gao W, Li J, Tam WY. Measuring circular phase-dichroism of chiral metasurface. Nanophotonics 2019;8:909.
[18] Plum E, Liu X-X, Fedotov VA, Chen Y, Tsai DP, Zheludev NI. Metamaterials: optical activity without chirality. Phys Rev Lett 2009;102:113902.
[19] Plum E, Zheludev NI. Chirality and anisotropy of planar metamaterials. In: Maradudin AA, editor. Structured surfaces as optical metamaterials. Cambridge, UK, Cambridge University Press, 2011:94–157.
[20] Fernandez-Corbaton I, Fruhnert M, Rockstuhl C. Objects of maximum electromagnetic chirality. Phys Rev X 2016;6:031013.
[21] Garcia-Santiago X, Burger S, Rockstuhl C, Fernandez-Corbaton I. Measuring the electromagnetic chirality of 2d arrays under normal illumination. Opt Lett 2017;42:4075–8.
[22] Kuwata-Gonokami M, Saito N, Ino Y, et al. Giant optical activity in quasi-two-dimensional planar nanostructures. Phys Rev Lett 2005;95:227401.
[23] Wu C, Arju N, Kelp G, et al. Spectrally selective chiral silicon metasurfaces based on infrared fano resonances. Nat Commun 2014;5:3892.
[24] Ye W, Yuan X, Guo C, Zhang J, Yang B, Zhang S. Large chiroptical effects in planar chiral metamaterials. Phys Rev Appl 2017;7:054003.
[25] Zhu AY, Chen WT, Zaidi A, et al. Giant intrinsic chiro-optical activity in planar dielectric nanostructures. Light Sci Appl 2018;7:17158.
[26] Zhao R, Sain B, Wei Q, et al. Multichannel vectorial holographic display and encryption. Light Sci Appl 2018;7:95.
[27] Arbabi A, Horie Y, Bagheri M, Faraon A. Dielectric metasurfaces for complete control of phase and polarization with subwavelength spatial resolution and high transmission. Nat Nanotech 2015;10:937–43.
[28] Karakasoglu I, Xiao M, Fan S. Polarization control with dielectric helix metasurfaces and arrays. Opt Exp 2018;26:21664–74.
[29] Zhu AY, Chen W-T, Khorasaninejad M, et al. Ultra-compact visible chiral spectrometer with meta-lenses. APL Photon 2017;2:036103.
[30] Balthasar Mueller JP, Rubin NA, Devlin RC, Groever B, Capasso F. Metasurface polarization optics: independent phase control of arbitrary orthogonal states of polarization. Phys Rev Lett 2017;118:113901.
[31] Li G, Zhang S, Zentgraf T. Nonlinear photonic metasurfaces. Nat Rev Mat 2017;2:17010.
[32] Li A, Singh S, Sievenpiper D. Metasurfaces and their applications. Nanophotonics 2018;7:989.
[33] Kamali SM, Arbabi E, Arbabi A, Faraon A. A review of dielectric optical metasurfaces for wavefront control. Nanophotonics 2018;7:1041.
[34] Limonov MF, Rybin MV, Poddubny AN, Kivshar YS. Fano resonances in photonics. Nat Photon 2017;11:543–54.
[35] Fu YH, Kuznetsov AI, Miroshnichenko AE, Yu YF, Luk'yanchuk B. Directional visible light scattering by silicon nanoparticles. Nat Commun 2013;4:1527.

[36] Khanikaev AB, Wu C, Shvets G. Fano-resonant metamaterials and their applications. Nanophotonics 2013;2:247.
[37] Person S, Jain M, Lapin Z, Sáenz JJ, Wicks G, Novotny L. Demonstration of zero optical backscattering from single nanoparticles. Nano Lett 2013;13:1806–9.
[38] Kim J, Li Y, Miskiewicz MN, Oh C, Kudenov MW, Escuti MJ. Fabrication of ideal geometric-phase holograms with arbitrary wavefronts. Optica 2015;2:958–64.
[39] Hsu CW, Zhen B, Stone AD, Joannopoulos JD, Soljačić M. Bound states in the continuum. Nat Rev Mater 2016;1:16048.
[40] Koshelev K, Favraud G, Bogdanov A, Kivshar Y, Fratalocchi A. Nonradiating photonics with resonant dielectric nanostructures. Nanophotonics 2019;8:725.
[41] Collin S. Nanostructure arrays in free-space: optical properties and applications. Rep Prog Phys 2014;77:126402.
[42] Menzel C, Rockstuhl C, Lederer F. Advanced jones calculus for the classification of periodic metamaterials. Phys Rev A 2010;82:053811.
[43] Molesky S, Lin Z, Piggott AY, Jin W, Vucković J, Rodriguez AW. Inverse design in nanophotonics. Nat Photon 2018;12:659–70.
[44] Kalish AN, Komarov RS, Kozhaev MA, et al. Magnetoplasmonic quasicrystals: an approach for multiband magneto-optical response. Optica 2018;5:617–23.
[45] Arteaga O, Maoz BM, Nichols S, Markovich G, Kahr B. Complete polarimetry on the asymmetric transmission through subwavelength hole arrays. Opt Express 2014;22:13719–32.
[46] Vázquez-Lozano JE, Martínez A. Optical chirality in dispersive and lossy media. Phys Rev Lett 2018;121:043901.
[47] Alpeggiani F, Bliokh KY, Nori F, Kuipers L. Electromagnetic helicity in complex media. Phys Rev Lett 2018;120:243605.
[48] Tang Y, Cohen AE. Optical chirality and its interaction with matter. Phys Rev Lett 2010;104:163901.
[49] Tang Y, Cohen AE. Enhanced enantioselectivity in excitation of chiral molecules by superchiral light. Science 2011;332:333–6.
[50] Mun J, Rho J. Importance of higher-order multipole transitions on chiral nearfield interactions. Nanophotonics 2019;8:941.
[51] Ge L, Feng L. Contrasting eigenvalue and singular-value spectra for lasing and antilasing in a $\mathcal{PT}$-symmetric periodic structure. Phys Rev A 2017;95:013813.
[52] Bai B, Svirko Y, Turunen J, Vallius T. Optical activity in planar chiral metamaterials: theoretical study. Phys Rev A 2007;76:023811.
[53] Bai B, Konishi K, Meng X, et al. Mechanism of the large polarization rotation effect in the all-dielectric artificially chiral nanogratings. Opt Exp 2009;17:688–96.
[54] Ossikovski R. Interpretation of nondepolarizing Mueller matrices based on singular-value decomposition. J Opt Soc Am A 2008;25:473–82.
[55] Arteaga O, Canillas A. Pseudopolar decomposition of the Jones and Mueller-Jones exponential polarization matrices. J Opt Soc Am A 2009;26:783–93.
[56] Ossikovski R, Kuntman MA, Arteaga O. Anisotropic integral decomposition of depolarizing Mueller matrices. OSA Continuum 2019;2:1900–7.

Supplementary Material: The online version of this article offers supplementary material (https://doi.org/10.1515/nanoph-2019-0321).